Adaptive Harmonic Tracking Based Speed Ripple Reduction Method for Permanent Magnet Synchronous Motor Drives

Siqi Wang, Binxing Li, *Member, IEEE*, Guoqiang Zhang, *Senior Member, IEEE*, Gaolin Wang, *Senior Member, IEEE*, Jianbing Chen, Jiangtao Yu, and Dianguo Xu, *Fellow, IEEE*

***Abstract*—In permanent magnet synchronous motor (PMSM) drive systems, nonideal factors induce periodic speed ripples. Conventional harmonic injection–based speed ripple reduction methods exhibit significant sensitivity to speed-loop bandwidth limitations and speed sensor sampling delays. According to the phase delay modeling in velocimetry and the equivalent cutoff frequency of the drive system, theoretical boundaries for the unstable operating region of harmonic injection–based methods are established. In this article, a novel speed ripple reduction method based on adaptive harmonic tracking is proposed for PMSM drives. The proposed method utilizes the saturation characteristics of spectral analysis theory under unstable states to adaptively correct the injected harmonic modes. The injected compensation current realizes adaptive tracking of speed ripple even in the presence of unmodeled disturbances. The effectiveness of the proposed method is verified by experiments on a 2.2-kW PMSM drive platform.**

***Index Terms*—Adaptive phase correction, closed-loop Fourier transform (CFT), permanent magnet synchronous motor (PMSM), speed ripple reduction.**

I. Introduction

PERMANENT magnet synchronous motors (PMSM) are widely adopted in fields such as household appliances, industrial, aerospace, and others due to the advantages of high power density, high reliability, and fast dynamic response [1], [2], [3], [4], [5]. In applications where the smoothness of the motor is highly required, e.g., robot arms, electric vehicles, and lift traction machines, the speed ripple will affect the stability and safety of the system [6], [7], [8]. Therefore, the speed ripple reduction algorithm for PMSM drives with a simple structure, high reliability, and good general performance has been a hot research topic for scholars in recent years [9], [10], [11].

Received 20 March 2025; revised 29 May 2025; accepted 5 July 2025. Date of publication 11 July 2025; date of current version 27 August 2025. This work was supported by the Research Fund for the National Natural Science Foundation of China under Grant 524B2098 and Grant 52125701. Recommended for publication by Associate Editor G. Scelba. *(Corresponding author: Binxing Li.)*

Siqi Wang, Binxing Li, Guoqiang Zhang, Gaolin Wang, and Dianguo Xu are with the School of Electrical Engineering and Automation, Harbin Institute of Technology, Harbin 150001, China (e-mail: 21b906039@stu.hit.edu.cn; li_binxing@163.com; zhgq@hit.edu.cn; wgl818@hit.edu.cn; xudiang@hit.edu.cn).

Jianbing Chen and Jiangtao Yu are with Qingdao Innovation Intelligent Appliance Research Institute Company Ltd., Qingdao 266000, China (e-mail: chenjb.gc@gczx.cn; yujt@gczx.cn).

Color versions of one or more figures in this article are available at https://doi.org/10.1109/TPEL.2025.3588522.

Digital Object Identifier 10.1109/TPEL.2025.3588522

Inverter nonlinearity, current harmonics, phase unbalance, back electromotive force harmonics, and load torque pulsations are the main causes of torque pulsation, which is a rich source of noise in the motor control system [12]. The design of speed ripple reduction algorithms often needs to consider a variety of noise sources, which places a high demand on the overall performance [13]. At present, the researches in the direction of speed ripple reduction mainly focus on the optimization design of the motor and the design of the control algorithm.

The motor design scheme primarily focuses on suppressing cogging torque and magnetic flux harmonics through optimization of the skewed slots, shifted teeth, pole arc coefficient design, and the use of auxiliary slots or teeth [14], [15], [16]. In [15], an air-gap optimization method based on grid search was proposed, which reduces the radial force acting on the stator teeth and the equivalent stress in the structure. By analyzing the intrinsic relationship between cogging torque and speed ripple, an adaptive step finite element analysis method was employed to optimize the rotor surface shape [16].

The control algorithms of speed ripple reduction can be mainly divided into two categories: the observer-based methods [17], [18], [19], [20], [31], [32], [33], [34] and the harmonic injection-based methods [21], [22], [23], [24], [25]. The harmonic observers are constructed based on the motor's mathematical model. By analyzing the effect of cogging torque on speed ripple, a virtual cogging torque observer was designed to achieve smooth speed control by online moving compensation of the stable point [17]. In [19], a phase lag compensation function was introduced into the repetitive controller, which effectively suppresses speed harmonics caused by dead-time settings. The above methods focus on velocity variations caused by a single disturbance. To further increase the versatility of the algorithm, some researchers have incorporated repetitive control into active disturbance rejection control algorithms [20], which allows the simultaneous suppression of harmonic disturbances introduced by different sources of interference.

The harmonic injection-based speed ripple reduction method, utilizing spectral analysis theory, relies less on the motor model and can reduce speed ripple without distinguishing harmonic sources. The forms of injected signals are mainly current injection and voltage injection. In [21], the compensated harmonic currents were injected into the q-axis currents based on motor modeling to achieve the suppression of torque pulsation caused

by current harmonics. The relationship between the current and the voltage harmonic injection was derived in [22]. Based on this, a hybrid injection method was proposed to avoid the oscillation problem caused by unstable. To improve the generalized performance of the harmonic injection method, a harmonic injection-based speed ripple reduction method with adaptive compensation for phase and amplitude based on the equivalent phase delay of the control system was developed [25]. Compared to the proportional resonant controller, this method shows better phase tracking stability.

It should be noted that the speed ripple consists of two components: the ripple amplitude and the ripple phase. Most existing research primarily focuses on the former. These approaches typically extract the fluctuating components from the speed signal to compute compensation values. Therefore, the accuracy and real-time performance of the encoder used for velocimetry determine the control performance [26]. With the incremental encoder, methods such as M method, T method, and M/T method are commonly used for PMSM drive systems. These three velocity measurement methods follow the idea of sliding average filtering [27]. As the measurement time or distance increases, the velocimetry accuracy improves. However, this also increases the measurement phase delay for the speed ripple. To improve the disturbance rejection of the speed controller, a low-pass filter with a lower cutoff frequency is cascaded to filter the speed feedback signal, thereby eliminating the sinusoidal ripple components in the speed [28]. In summary, the current researches mainly focus on the accuracy analysis of velocimetry algorithms, with limited studies on the phase lag problem introduced by these algorithms.

This article proposes a speed ripple reduction method based on adaptive harmonic tracking, aiming to enhance disturbance rejection ability against fluctuating load torque in PMSM drives. The theoretical boundaries for the unstable region of harmonic injection-based speed ripple reduction methods are established through coupled dynamics analysis between the phase delay modeling in velocimetry and the equivalent cutoff frequency of the drive system. The proposed method utilizes the saturation characteristics of spectral analysis theory under unstable states to adaptively correct the injected harmonic modes. By adaptively correcting the system phase-frequency characteristics, unstable issues caused by the cutoff frequency are avoided. Also, the injected compensation current realizes adaptive tracking of speed ripple even in the presence of unmodeled disturbances. The effectiveness of the proposed method is verified by experiments on a 2.2-kW PMSM platform. The compensated system demonstrates enhanced stability margins in the full speed range.

II. Analysis of the Impact of Velocimetry Delay on System Stability

A. Modeling of Phase Delay Introduced By Velocimetry

In PMSM drives, typical methods of motor velocimetry based on incremental encoder are the M method, the T method, and a combination of both, referred to as the M/T method. When periodic speed ripples are present in the motor system, the speed ripple reduction method needs to extract the fluctuation information from the rotor speed obtained by the velocity algorithm. However, the velocity algorithm based on the moving average theory will introduce a phase delay in the measurement of fluctuating signals, which affects the control performance of the speed ripple reduction method. This problem will exacerbate as the frequency of speed ripple increases.

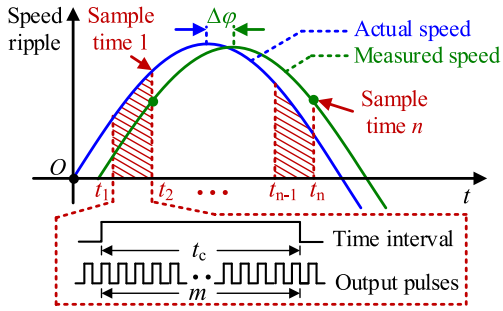

Fig. 1. Schematic diagram of phase delay introduced by velocimetry.

Taking the M method as an example for modeling analysis, the rotor speed is calculated by counting the number of encoder output pulses m within a certain time interval t_c. If the motor encoder generates z pulses per revolution, the measured speed n_{eM} can be expressed as

$$n_{eM} = 60\ m/zt_c. \tag{1}$$

To improve observation accuracy, t_c cannot be smaller, as this introduces a phase lag $\Delta\varphi$ in the speed calculation, particularly in the presence of speed ripple, as shown in Fig. 1.

According to the Fourier expansion theory, any periodic ripple can be expanded into a sum of sine and cosine functions. Let the speed ripple be $n_{real} = A_n \sin(2\pi f_n t)$, where A_n and f_n are the amplitude and the frequency of the actual speed ripple, respectively. The measured speed ripple n_{eM} calculated at n moments is

$$\begin{aligned} n_{eM} &= \int_{t_{n-1}}^{t_n} A_n \sin(2\pi f_n t)\mathrm{d}t \\ &= \frac{A_n}{\pi f_n t_c} \cdot \sin(\pi f_n t_c) \cdot \sin\left[\pi f_n (t_{n-1} + t_n)\right]. \end{aligned} \tag{2}$$

It can be seen from (2) that a smaller sampling period brings the measured speed closer to the actual value. However, reducing the sampling period also reduces velocimetry accuracy. By comparing the phase relationship between the actual speed ripple and the speed ripple obtained from velocimetry, $\Delta\varphi$ introduced by velocimetry can be calculated as

$$\Delta\varphi = 2\pi f_n t_n - \pi f_n (t_{n-1} + t_n) = \pi f_n t_c. \tag{3}$$

According to [29], the transfer function of phase delay $G_{eM}(s)$ introduced by velocimetry can be expressed as

$$G_{eM}(s) = \left(\frac{1 - e^{-s \cdot t_c}}{s \cdot t_c}\right)^2. \tag{4}$$

According to (4), set the sampling time t_c to 2 ms and plot the Bode diagram of the phase delay introduced by velocimetry, as

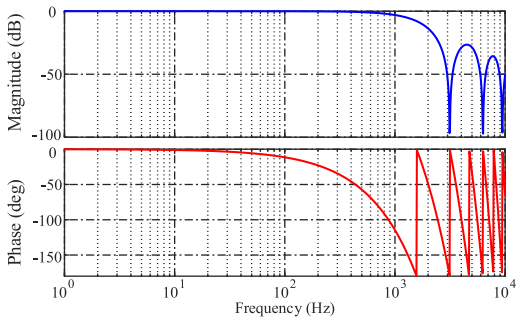

Fig. 2. Bode diagram of phase delay introduced by velocimetry.

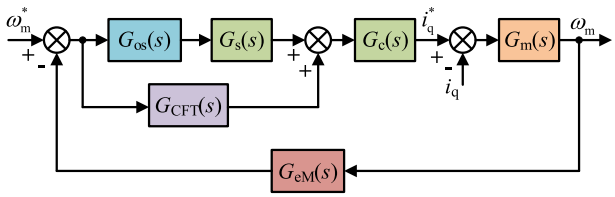

Fig. 3. Schematic diagram of phase delay introduced by velocimetry.

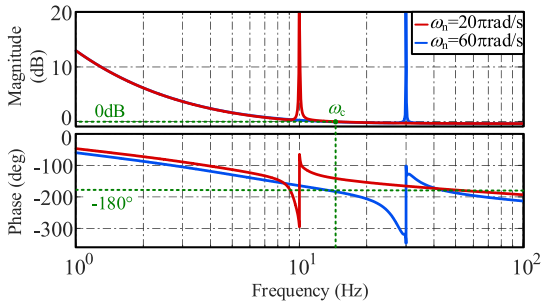

Fig. 4. Bode diagram of the speed control system.

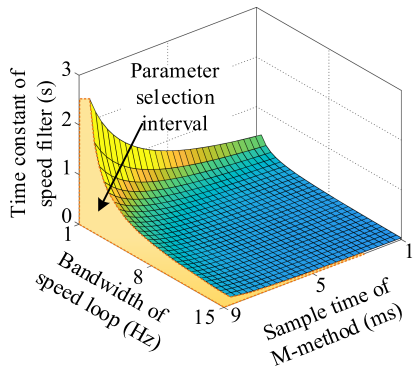

Fig. 5. Parameter selection region for the speed control system.

shown in Fig. 2. As shown in Fig. 2, the phase lag increases progressively with motor speed, whereas the amplitude attenuation remains largely unchanged.

B. Stability Analysis of Harmonic Injection-Based Method

Due to factors such as the dead-time setting and fluctuating load torque disturbances, speed ripples are commonly observed in motor control systems. The speed controllers are typically unable to suppress these harmonics due to the limited bandwidth. And owing to the velocimetry delays, there is a phase lag between the actual speed ripple and the extracted signal used for the harmonic injection-based speed ripple reduction method. Excessive phase delay can lead to unstable of the control system.

Taking the closed-loop Fourier transform (CFT)-based speed ripple reduction method as an example, the block diagram of the transfer function of the speed closed-loop control system is shown in Fig. 3.

In Fig. 3, ω_{m} and $\omega*$ m are the actual and the given speed, respectively. i_{q} and $i*$ q are the actual and the given q-axis current, respectively. $G_{\mathrm{os}}(s) = 1/(\tau_{\mathrm{os}}s{+}1)$ is the transfer function of the velocity feedback filter, where τ_{os} is the velocity feedback filter time constant. $G_{\mathrm{s}}(s) = 1/(\tau_{\mathrm{s}}s{+}1)$ is the transfer function of the speed loop proportional integral (PI) controller, where τ_{s} is the speed loop time constant. $G_{\mathrm{c}}(s) = 1/(\tau_{\mathrm{c}}s{+}1)$ is the transfer function of the current loop PI controller, where τ_{c} is the current loop time constant. $G_{\mathrm{m}}(s) = K_{\mathrm{t}}/(Js{+}B)$ is the transfer function of a mechanical system, where K_{t}, J, and B represent the motor mechanical time constant, moment of inertia, and friction coefficient, respectively. $G_{\mathrm{CFT}}(s)$ is the transfer function of the CFT-based method, as described in [30], and can be expressed as

$$G_{\mathrm{CFT}}(s) = -\frac{k_{\mathrm{p}}s^3+(k_{\mathrm{p}}+k_{\mathrm{i}})s^2+(k_{\mathrm{p}}\omega_n^2+k_{\mathrm{i}})s+(k_p-k_{\mathrm{i}})\omega_n^2}{s^4+2s^3+(1+2\omega_n^2)s^2+2\omega_n^2 s+\omega_n^2+\omega_n^4} \tag{5}$$

where k_{p} and k_{i} are the proportional and integral parameters of the CFT-based method, respectively, and ω_{n} is the center frequency.

To analyze the system's stability, the open-loop transfer function $G_{\mathrm{OL}}(s)$ of the speed control system is derived as (8) shown at the bottom of the next page. It can be seen from (8) that there is no positive pole in the system open-loop transfer function ($P = 0$). By substituting the motor parameters from Table II into (8), the Bode diagram is plotted at center frequencies of 20π rad/s and 60π/s rad, as shown in Fig. 4.

In Fig. 4, according to the system stability criterion, in the frequency range before the system cutoff frequency ω_{c}, the phase-frequency characteristic curve at 20π rad/s exhibits a positive crossing (N_+) and a negative crossing (N_-) at the $-180°$ line, indicating system stability. However, at 60π rad/s, the phase–frequency characteristic curve shows only one negative crossing (N_-) at the $-180°$ line, indicating system instability.

From the above analysis, it can be seen that the phase delay introduced by the velocimetry delay, the control loop bandwidth, and system nonideal characteristics will all lead to system instability.

To ensure that the system does not operate in a critically stable state, the phase margin γ is designed as

$$\angle G_{\mathrm{OL}}(j\omega_{\mathrm{c}}) - \gamma > -\pi. \tag{6}$$

TABLE I
DIFFERENCE BETWEEN THE PROPOSED AND THE EXISTING SPEED RIPPLE REDUCTION METHOD

Type	Features	Concerns
Extended state observer [31]	- Less dependence on accurate modeling - Strong robustness	- Sensitive to parameter tuning - Limited ability to distinguish harmonic frequencies
Disturbance observer [32]	- Conceptually clear and intuitive - Harmonious balance of performance characteristic	- Complicated control law design
Sliding mode observer [33]	- Easy to implement - Excellent dynamic performances	- Chattering phenomenon - Infinite-time convergence
Internal model control [34]	- Two degrees of freedom control design for trajectory tracking and disturbance rejection	- Restricted control performance under complex disturbance conditions
The proposed method	- Excellent parameter robustness. - Good harmonic tracking capability	- Offline determination of frequency for harmonic suppression

TABLE II
PARAMETERS OF THE TEST PMSM

Parameter	Value	Parameter	Value
Rated power	2.2 kW	Phase resistance	2.53 Ω
Rated voltage	380 V	D-axis inductance	22.38 mH
Rated current	3.5 A	Q-axis inductance	51.75 mH
Rated frequency	75 Hz	Pairs of poles	3
Rated speed	1500 r/min	Magnetic flux	0.5 Wb

When the motor operates at low speed, the phase lag introduced by the current loop and mechanical system can be neglected. Substituting (3) and (5) into (6) yields

$$\tau_{\mathrm{os}} < \frac{\tan\left[\left(0.75 - f_n t_{\mathrm{c}}\right)\pi - \gamma\right]}{\omega_{\mathrm{c}}}, \quad \gamma > \tfrac{1}{4}\pi. \tag{7}$$

According to (7), the relationship between the speed loop bandwidth, speed feedback filter time constant, and M-method sampling time is plotted, as shown in Fig. 5. It can be seen that, to ensure the system meets the required phase margin γ in (6), a complex offline testing and tuning process is required that reduces overall performance.

In Section II, the theoretical boundaries for the unstable region of harmonic injection-based speed ripple reduction methods are established through coupled dynamics analysis. At the same time, this section innovatively points out that the phase delay introduced by velocimetry will seriously affect the stability of the harmonic injection-based method through phase delay modeling of the velocimetry system and control system stability analysis. The solution to this problem will be introduced in the next section.

III. PROPOSED ADAPTIVE HARMONIC TRACKING BASED SPEED RIPPLE REDUCTION METHOD

A. Principle of Adaptive Harmonic Tracking Method

To solve the problem mentioned in Section II, a speed ripple reduction method based on adaptive harmonic tracking is proposed in this article, as shown in Fig. 6. This method does not require distinguishing the sources of speed ripple, avoiding the complexity of the parameter and convergence design process. Meanwhile, the proposed method is unaffected by the speed loop bandwidth and phase lag introduced by velocimetry, offering advantages such as a simple structure and strong versatility.

The proposed method can be divided into two parts: a CFT extraction module and an adaptive phase correction function. The former is responsible for extracting harmonic information from the speed ripple and preliminarily generating the compensation current. The latter is responsible for adaptively correcting the phase lag of the compensation current. By setting the central frequency ω_{m} of the sine and cosine functions to be consistent with the harmonic frequency that needs to be suppressed, this method has a good suppression effect on any frequency harmonic order.

The motor speed ω_{m} varies periodically due to various non-ideal factors of control systems, which can be expressed as

$$\omega_{\mathrm{m}}(t) = \omega_0(t) + \sum_{k=1}^{+\infty}\left[A_{\omega\mathrm{ck}}\cos\left(k\omega_{\mathrm{m}}t\right) + A_{\omega\mathrm{sk}}\sin\left(k\omega_{\mathrm{m}}t\right)\right] \tag{9}$$

where ω_0, $A_{\omega\mathrm{ck}}$, and $A_{\omega\mathrm{sk}}$ are the dc component of ω_{m} and the cosine and the sine Fourier decomposition amplitudes of the kth harmonic component of ω_m, respectively.

$$\begin{aligned} G_{\mathrm{OL}}(s) &= \left[G_{\mathrm{os}}(s)\,G_{\mathrm{s}}(s) + G_{\mathrm{CFT}}(s)\right]\cdot G_c(s)\,G_{\mathrm{m}}(s)\,G_{\mathrm{eM}}(s) \\ &= \frac{K_{\mathrm{t}}}{(Js+B)(\tau_{\mathrm{c}}s+1)}\left(\frac{1}{(\tau_{\mathrm{os}}s+1)(\tau_{\mathrm{s}}s+1)} - \frac{k_{\mathrm{p}}s^3+(k_{\mathrm{p}}+k_{\mathrm{i}})s^2+(k_{\mathrm{p}}\omega_n^2+k_{\mathrm{i}})s+(k_{\mathrm{p}}-k_{\mathrm{i}})\omega_n^2}{s^4+2s^3+(1+2\omega_n^2)s^2+2\omega_n^2 s+\omega_n^2+\omega_n^4}\right)\left(\frac{1-e^{-s\cdot t_{\mathrm{c}}}}{s\cdot t_{\mathrm{c}}}\right)^2. \end{aligned} \tag{8}$$

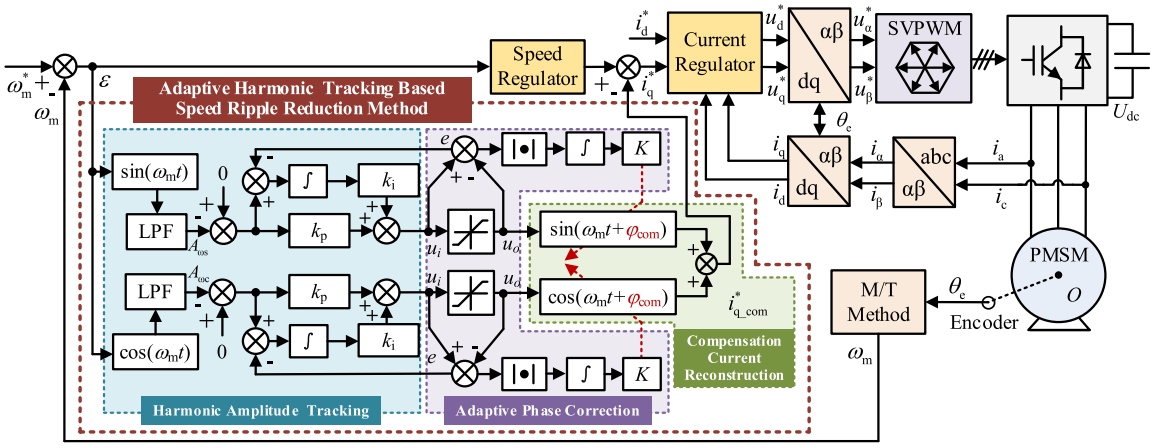

Fig. 6. Proposed adaptive harmonic tracking based speed ripple reduction method for PMSM drives.

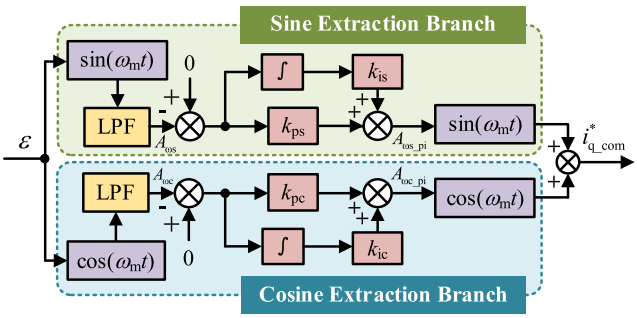

Fig. 7. Block diagram of the CFT method.

To enhance the harmonic extraction capability, the CFT method is adopted, as shown in Fig. 7. The basic idea of the CFT method is to generate a fluctuating $i^*_{q\_com}$ by extracting the fluctuating component from ω_m. $A_{\omega ck}$ and $A_{\omega sk}$ can be extracted from the speed error ε through the Fourier transform. A sinusoidal compensation current $i^*_{q\_com}$ is generated by combining the adjustable compensation angle φ_{com} and the compensation gain K, which has the same frequency as the extracted harmonic. By setting the rotation frequency of the sine and cosine functions to be consistent with the harmonic frequency that needs to be suppressed, this method has a good suppression effect on any harmonic frequency order.

Taking the fundamental component ($k = 1$) harmonic as an example. Multiplying the speed error ε by the sine and the cosine component of the rotor position, the following can be obtained as

$$\begin{cases} \varepsilon(t)\cdot\sin(\omega_m t) = (\omega_m-\omega_0)\cdot\sin(\omega_m t) \\ \quad \approx [A_{\omega c}\cos(\omega_m t)+A_{\omega s}\sin(\omega_m t)]\cdot\sin(\omega_m t) \\ = \frac{1}{2}A_{\omega s}+\frac{1}{2}[A_{\omega s}\sin(2\omega_m t)-A_{\omega c}\cos(2\omega_m t)] \\ \varepsilon(t)\cdot\cos(\omega_m t) = (\omega_m-\omega_0)\cdot\cos(\omega_m t) \\ \approx [A_{\omega c}\cos(\omega_m t)+A_{\omega s}\sin(\omega_m t)]\cdot\cos(\omega_m t) \\ = \frac{1}{2}A_{\omega c}+\frac{1}{2}[A_{\omega c}\cos(2\omega_m t)+A_{\omega s}\sin(2\omega_m t)] \end{cases} \tag{10}$$

where $A_{\omega c}$ and $A_{\omega s}$ are the cosine and the sine Fourier decomposition amplitude of the fundamental component of speed error ε (t), respectively.

When the harmonic frequency is identified, the sine/cosine functions and low-pass filters in the amplitude extraction stage are employed to extract the amplitude of the speed ripple. Taking the sine branch as an example, (11) is obtained as

$$A_{\omega s} = \frac{1}{2\pi}\int_{-\infty}^{+\infty}[\varepsilon(t)\cdot\sin(\omega_m t)]\frac{1}{T_f j\omega+1}e^{j\omega t}d\omega. \tag{11}$$

Excessive phase delay can lead to unstable of the control system. When the injected signal is miscompensated, it will cause the CFT method to diverge until the controller is saturated. In other words, as long as the integrator is saturated, it means that there is a certain phase lag in the system that needs to be compensated. When the phase lag compensation is completed, the algorithm will exit the saturation region. Therefore, whether the algorithm enters the saturation region becomes a sign of whether phase compensation is needed.

The adaptive extraction of the compensation amplitude and phase is achieved through a PI controller with antiwindup function. The control law can be expressed as

$$u_i = -\begin{cases} k_p A_{\omega s}+\int k_i A_{\omega s}dt, & u_i \le u_o \\ k_p A_{\omega s}+\int k_i[A_{\omega s}-(u_i-u_o)]dt, & u_i > u_o \end{cases} \tag{12}$$

where u_i and u_o represent the input and output value of the integral limiter. By utilizing the phase error information, when the algorithm operates in the saturation region, the compensation phase φ_{com} is adaptively corrected through saturation characteristic extraction as

$$\varphi_{com} = \begin{cases} \int K|u_i-u_o|dt, & u_i \le u_o \\ \int K|u_i-U_o\cdot\mathrm{sgn}(u_i)|dt, & u_i > u_o \end{cases} \tag{13}$$

where U_o represents the upper limit of the antiwindup controller, sgn($\cdot$) denotes the sign function, and K represents the self-tuning parameter, whose value influences the speed of adaptive adjustment.

By extracting saturation information, the compensation phase φ_{com} in (13) is gradually approached to the phase lag $\Delta\varphi$ introduced by velocimetry in (3) to achieve adaptive harmonic tracking.

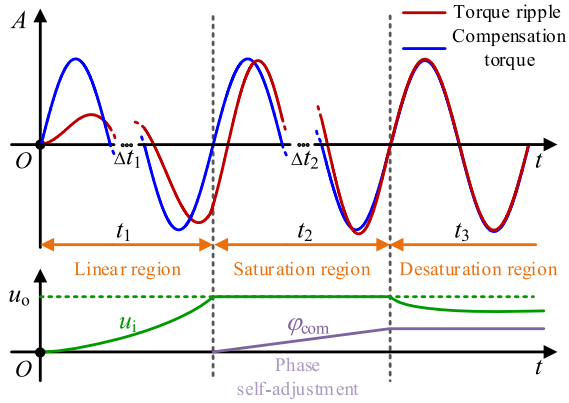

Fig. 8. Operating modes of the proposed strategy.

It can be seen from (13) that, when the system is stable ($u_i = u_o$), the compensation angle is 0. When the system operates in the saturation region ($u_i > u_o$), the proposed method utilizes the difference between the input and output of the saturation function to adaptively extract the compensation angle, and gradually accumulates the compensation angle until the system is stable ($u_i = u_o$). When it operates in the desaturation region, the adaptive convergence process of the delay phase angle is completed. From the convergence process, it can be seen that the proposed method does not rely on any motor parameters and has good generality.

After obtaining the compensation amplitude and phase for the sine/cosine branch, the two branches are combined to reconstruct the injected compensation harmonic current $i*$ q_com. By integrating (11)–(13), the control law of the proposed strategy can be derived as

$$\begin{cases} A_{\omega s} = \frac{1}{2\pi}\int_{-\infty}^{+\infty}\left[\varepsilon\cdot\sin\left(\omega_n t\right)\right]\frac{1}{T_f j\omega+1}e^{j\omega t}d\omega \\ u_i = -\begin{cases} k_p A_{\omega s} + \int k_i A_{\omega s} dt, & u_i \le u_o \\ k_p A_{\omega s} + \int k_i \left[A_{\omega s} - (u_i - u_o)\right] dt, & u_i > u_o \end{cases} \\ i^*_{q\_com} = u_o\left[\sin\left(\omega_n t + \int K\left|u_i - u_o\right| dt\right)\right. \\ \qquad\left. + \cos\left(\omega_n t + \int K\left|u_i - u_o\right| dt\right)\right] \end{cases} \tag{14}$$

where ω_n is the central frequency of the harmonic to be suppressed. It should be noted that ω_n can be the k (k = 1,2,3, …,) times at the mechanical speed ω_m, or it can be any fixed frequency that is independent of the speed. It can be seen from the control law that the proposed method does not depend on the motor parameters.

Based on spectrum analysis theory, when the injected signal is miscompensated, it will cause the system to diverge until the controller is saturated. This is the saturation characteristic of the system. The proposed method divides three control modes through the saturation function: linear region, saturation region, and desaturation region. A schematic diagram of the operating mode is shown in Fig. 8.

In the linear region, the compensation q-axis current is initially generated by the coordination of the closed-loop extraction branches. When in the saturation region, the control law is constructed in combination with the saturation characteristic of the system, and the compensation current phase is adaptively adjusted to achieve the best control effect. The injected compensation current realizes adaptive tracking of speed ripple even in the presence of unmodeled disturbances.

In summary, the proposed method utilizes the saturation characteristics of spectral analysis theory under unstable states to adaptively correct the injected harmonic modes. By adaptively correcting system phase-frequency characteristics, unstable issues caused by the cutoff frequency are avoided. Also, the injected compensation current realizes adaptive tracking of speed ripple even in the presence of unmodeled disturbances.

B. Analysis of the Attractivity Conditions

As shown in Fig. 8, the proposed algorithm usually operates in the linear region or desaturation region. When the fluctuating torque disturbance changes, the speed ripple reduction system may operate in the saturation region. In this region, the harmonic amplitude tracking function is blocked and the integral state tends to zero. If the fluctuation torque remains within a certain range, the system will be attracted from the saturation region to the desaturation region. Therefore, it is necessary to analyze the attraction conditions of the system from the saturation region to the desaturation region.

Since the time constant of the current controller is much smaller than that of the speed controller ($\tau_c << \tau_s$), the input error equation of the proposed algorithm is given by

$$J\dot{\varepsilon} = -B\varepsilon - JK_t i_{q\_com} + T'_L \tag{15}$$

where T'_L represents the load torque ripple. In the saturation and the desaturation region, the following holds:

$$\begin{aligned} i_{q\_com} &= u_o\left[\sin\left(\omega_m t + K\int\left|u_i - u_o\right| dt\right)\right. \\ &\quad\left. + \cos\left(\omega_m t + K\int\left|u_i - u_o\right| dt\right)\right] \\ &= \sqrt{2}u_o\sin\left(\omega_m t + 0.25\pi + \varphi_{com}\right). \end{aligned} \tag{16}$$

It should be noted that in the linear region, φ_{com} is 0, whereas in the desaturation region, φ_{com} is a constant value.

Defining the integrator output value as q, in the linear region, (17) can be obtained as

$$\dot{q} = A_{\omega s}k_i. \tag{17}$$

Constructing the Lyapunov function $V_1(\varepsilon, q)$ as

$$V_1(\varepsilon, q) = \frac{1}{2}\varepsilon^2 + \frac{1}{2}(q - q_s)^2 \tag{18}$$

where q_s represents the steady-state value of the integrator.

Substituting (15)–(17) into the derivative of (18) yields

$$\begin{aligned} V_1(\varepsilon, q) &= \varepsilon\dot{\varepsilon} + \dot{q}(q - q_s) \\ &= -\frac{B}{J}\varepsilon^2 - \sqrt{2}K_t\left(q + \frac{k_p}{k_i}\dot{q}\right)\sin\left(\omega_m t + \frac{\pi}{4}\right)\varepsilon \\ &\quad + \frac{T'_L}{J}\varepsilon + A_{\omega s}k_i(q - q_s). \end{aligned} \tag{19}$$

Let the maximum value function max{ε } represents the amplitude of the sinusoidal component of the speed ripple ε. To

maintain system stability ($V_1(\varepsilon, q) \le 0$), (20) can be obtained as

$$\frac{T'_{\mathrm{L}}}{J}\varepsilon + k_{\mathrm{i}}\left(q - q_{\mathrm{s}}\right)\cdot \max\left\{\varepsilon\right\} \le 0. \tag{20}$$

Since the system operates in the linear region, q_{s} should be less than the upper limit U_{o}. Rearranging (20) yields

$$T'_{\mathrm{L}} \le k_{\mathrm{i}} J\left(U_{\mathrm{o}} - q\right). \tag{21}$$

When the speed ripple, motor inertia, and integrator output value satisfy the relationship in (21), the proposed method operates in the linear region. When in the saturation region, the desaturation condition should be discussed.

Constructing the Lyapunov function $V_2(\varepsilon\ )$ as

$$V_2\left(\varepsilon\right) = \frac{1}{2}\varepsilon^2. \tag{22}$$

Substituting (15) and (16) into the derivative of (22) yields

$$\begin{aligned}\dot{V}_2\left(\varepsilon\right) &= \varepsilon\dot{\varepsilon}\\ &= -\frac{B}{J}\varepsilon^2 - \sqrt{2}\varepsilon u_{\mathrm{o}} K_{\mathrm{t}} \sin\left(\omega_{\mathrm{m}} t + \frac{\pi}{4} + \varphi_{\mathrm{com}}\right) + \frac{\varepsilon}{J} T'_{\mathrm{L}}.\end{aligned} \tag{23}$$

In the saturation state, the output of the integrator is zero. Therefore, after extracting the dc component through the low-pass filter, the input value can be expressed as $u_{\mathrm{i}} = A_{\omega \mathrm{s}} k_{\mathrm{p}}/2$. Setting the saturation upper limit as $u_{\mathrm{i}} = U_{\mathrm{o}}$, and the input value into (23) yields

$$\begin{aligned}\dot{V}_2\left(\varepsilon\right) =& -\frac{B}{J}|\varepsilon|^2 - \frac{\sqrt{2}}{2} U_{\mathrm{o}} K_{\mathrm{t}} \varepsilon \mathrm{sgn}(k_{\mathrm{p}} A_{\omega \mathrm{s}})\\ & \sin\left(\omega_{\mathrm{m}} t + \frac{\pi}{4} + \varphi_{\mathrm{com}}\right) + \frac{T'_{\mathrm{L}}}{J}\varepsilon\\ \le& -\frac{B}{J}|\varepsilon|^2 - |\varepsilon|\left(\frac{\sqrt{2}}{2} U_{\mathrm{o}} K_{\mathrm{t}} k_{\mathrm{p}} - \frac{T'_{\mathrm{L}}}{J}\right).\end{aligned} \tag{24}$$

To ensure system stability, according to the Lyapunov stability criterion, let $\dot{V}_2(\varepsilon) < 0$, which gives

$$|\varepsilon| \le \frac{T'_{\mathrm{L}}}{B} - \frac{\sqrt{2} J U_{\mathrm{o}} K_{\mathrm{t}} k_{\mathrm{p}}}{2B}. \tag{25}$$

In the desaturation region, the maximum error satisfying the attraction condition of the linear region should be less than the error constraint $U_{\mathrm{o}}/k_{\mathrm{p}}$. Rearranging (25) yields

$$T'_{\mathrm{L}} \le \left(\frac{B}{k_{\mathrm{p}}} + \frac{\sqrt{2} J K_{\mathrm{t}} k_{\mathrm{p}}}{2}\right) U_{\mathrm{o}}. \tag{26}$$

If the system satisfies the attraction condition in (26), the speed ripple will converge within the error boundary, and the proposed strategy will be attracted from the saturation region to the desaturation region.

C. Stability Analysis of the Desaturation Region

Depending on whether the desaturation algorithm is enabled, two regions exist: the linear region ($\omega < \omega_{\mathrm{c}}$) and the desaturation region ($\omega > \omega_{\mathrm{c}}$). The system transfer function in the linear region is consistent with (8). When the system operating frequency is lower than the cutoff frequency, according to Fig. 4, the system is stable. Otherwise, the system enters the saturation region.

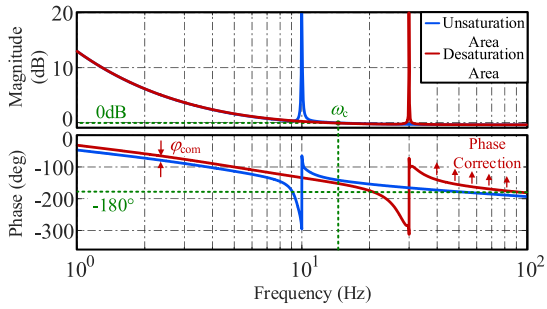

Fig. 9. Bode diagram of the proposed system.

This section analyzes the stability of the proposed method in the desaturation region. The low-pass filter adopts a first-order form with the cutoff frequency of 1 Hz, and its transfer function is given by $G_{\mathrm{LPF}}(s) = 1/(s{+}1)$. The system transfer function for the desaturation region is constructed as

$$\begin{cases} a(s) = -L\left[e(t)\sin(\omega_{\mathrm{m}} t)\right]\cdot G_{\mathrm{LPF}}(s)\cdot G_{\mathrm{PI}}(s)\\ b(s) = -L\left[e(t)\cos(\omega_{\mathrm{m}} t)\right]\cdot G_{\mathrm{LPF}}(s)\cdot G_{\mathrm{PI}}(s)\\ i^*_{\mathrm{q\_com}}(s) = L\left[a(t)\sin\left(\omega_{\mathrm{m}} t + \varphi_{\mathrm{com}}\right) + b(t)\cos\left(\omega_{\mathrm{m}} t + \varphi_{\mathrm{com}}\right)\right] \end{cases} \tag{27}$$

where $L(\cdot)$ denotes the Laplace transform operator.

Rearranging (27) yields

$$G'_{\mathrm{CFT}}\left(s\right) = G_{\mathrm{CFT}}\left(s\right) e^{-\varphi_{\mathrm{com}} s}. \tag{28}$$

Substituting (28) into (8), the open-loop transfer function of the control system in the desaturation region is obtained as (29) shown at the bottom of the next page.

Based on (29), the open-loop transfer function of the proposed method is plotted, as shown in Fig. 9.

According to the system stability criterion, it can be seen that the proposed strategy stabilizes the control system after desaturation by adaptively adjusting the lead phase. This theoretically resolves the divergence issue of the speed ripple reduction caused by the phase lag introduced by speed sampling. By comparing the Bode diagrams of the open-loop transfer functions of the traditional method in Fig. 4 and the proposed method in Fig. 9, the effectiveness of the proposed method is verified.

To describe the difference between the proposed method and the existing speed ripple reduction methods more intuitively, a detailed comparison is listed in Table I.

D. Parameter Tuning for Speed Ripple Minimization

The design of the parameter k_{i} is analyzed based on the characteristics of the controller in the linear region. According to (5), let the open-loop gain be G_0, and the following holds

$$G_0 = 20\lg\left|G_{\mathrm{CFT}}\left(s\right)\right|_{s=j\omega_n}. \tag{30}$$

Since the parameters U_{o}, k_{p}, and K determine the desaturation and phase adaptive adjustment speed of the algorithm in the saturation region, the design of these parameters needs to be

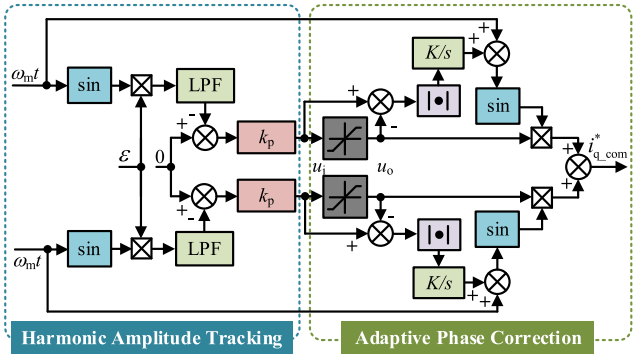

Fig. 10. Control block diagram of the proposed strategy under integrator saturation conditions.

analyzed in the saturation region. Fig. 10 shows the simplified control block diagram of the proposed strategy under saturation conditions.

To ensure the algorithm can smoothly transition from the saturation region to the linear region, the range of the saturation region limit value U_o is derived by referencing (26) as

$$U_o \geq \frac{2k_p T'_L}{2B + \sqrt{2} J K_t k_p^2}. \tag{31}$$

As shown in Fig. 10, the proposed phase adaptive algorithm primarily involves the lead correction of the compensation current. Without correction, let $i_{q\_com}(t) = \sqrt{2}\, u_o \sin(\omega_m t + 0.25\pi)$. Based on the time-shift property of the Laplace transform, the expression for the q-axis current in the complex frequency domain after compensation $i*$ q_com(s) can be obtained as

$$i'_{q\_com}(s) = L\left[i_{q\_com}\left(t + \frac{\varphi_{com}}{\omega_m}\right)\right] = \sqrt{2} u_o \frac{\omega_m}{s^2 + \omega_m^2} e^{\left(\frac{\pi}{4} + \frac{K A_\omega k_i}{2s}\right)s}. \tag{32}$$

It can be seen from (32) that the proposed method focuses on the adaptive correction of the compensation phase. Considering the sinusoidal ripple component in the mechanical equation of the PMSM, (33) can be obtained as

$$A_\omega = \frac{3 n_p \psi_m A_{iq}}{2 J \omega_m} \tag{33}$$

where A_{iq} represents the amplitude of the q-axis current ripple component. Considering the inverse relationship between the phase compensation value and the amplitude of the q-axis current ripple component, A_{iq} can be derived $A_{iq} = i_b(1\text{-}\varphi_{com}/\pi)$, where i_b is the current base value.

To tune the phase correction parameter K, it is necessary to construct a phase correction system control block diagram with the speed fluctuation A_ω as the control target. The simplified system block diagram is shown in Fig. 11. As shown is Fig. 11,

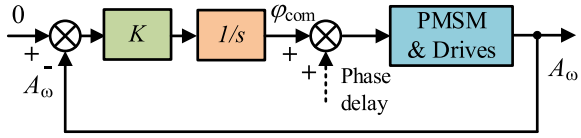

Fig. 11. Simplified block diagram of phase correction system.

the phase correction system can be equivalent to a first-order system. Taking $\varphi_{com}(s)$ as the control target, the transfer function of can be obtained as

$$\varphi_{com}(s) = \frac{3\pi n_p \psi_m i_b K}{-2\pi J \omega_m s + 3 n_p \psi_m i_b K}. \tag{34}$$

Defining the time constant of this system as τ_{phase}, the theoretical value of the phase correction parameter K can be obtained as

$$K = \frac{2\pi J \omega_m}{3 n_p \psi_m i_b \tau_{phase}}. \tag{35}$$

Through the tuning process of parameters k_i, U_o, and K in (30), (31), and (35), it can be seen that the proposed method has little dependence on motor parameters. It should be noted that, as can be seen from (33), as the motor inertia changes, the harmonics in the control system will also change accordingly, which puts higher requirements on the speed ripple reduction method. To address this problem, the proposed method matches the optimal compensation current through a method similar to online optimization. The proposed algorithm has good robustness in the case of parameter mismatch.

IV. Experimental Results

To verify the effectiveness of the proposed speed ripple reduction method, experiments were performed on the 2.2-kW PMSM platform shown in Fig. 12. The parameters of the test PMSM are listed in Table II. An induction motor is coaxially fixed with the PMSM to produce the load torque. An ARM chip STM32F103VCT6 is applied to execute the entire control strategy. The PWM carrier frequency and the sampling frequency are all set to 6 kHz. The parameters of the proposed method are set to $k_i = 25$, $k_p = 2$, and $K = 0.1$.

The position was obtained from an OMRON E6B2-CWZ6C 2000P/R incremental encoder. To maintain the velocimetry accuracy while taking into account the measurement noise problem, the sampling time interval t_c should not be too long or too short, and is set to 10 ms.

According to (3), when the motor operates at 700 r/min and 300 r/min, the velocimetry lag of the ripple harmonic at twice the mechanical speed is calculated to be 0.23π rad and 0.10π rad, respectively.

$$\begin{aligned} G'_{OL}(s) &= \left[G_{os}(s) G_s(s) + G_{CFT}(s)\right] \cdot G_c(s) G_m(s) G_{eM}(s) \\ &= \frac{K_t}{(Js + B)(\tau_c s + 1)} \cdot \left(\frac{1 - e^{-s \cdot t_c}}{s \cdot t_c}\right)^2 \cdot \left(\frac{1}{(\tau_{os} s + 1)(\tau_s s + 1)} - G_{CFT}(s)\, e^{-\varphi_{com} s}\right). \end{aligned} \tag{29}$$

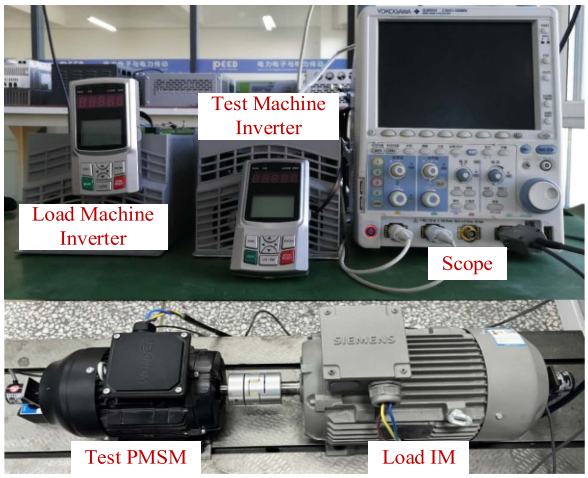

Fig. 12. Experimental platform of 2.2-kW PMSM.

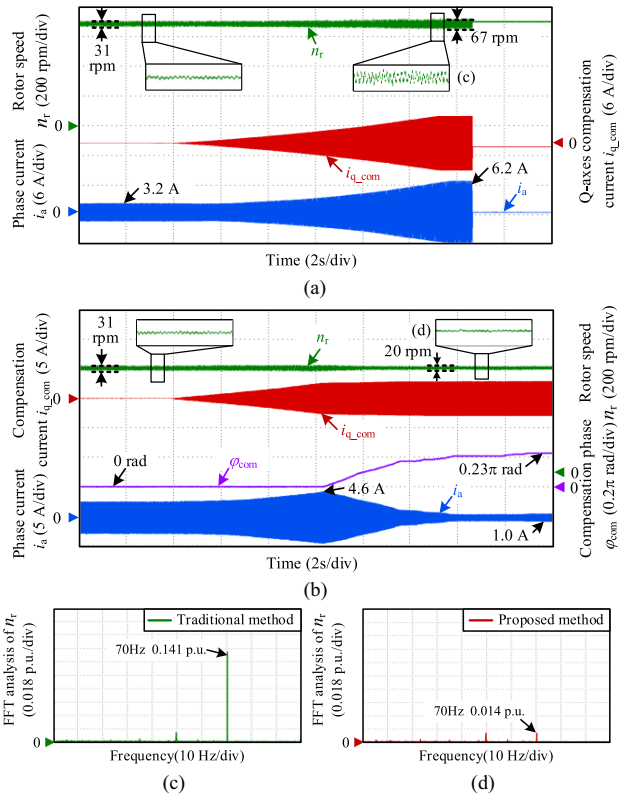

Fig. 13. Experimental comparison results and Fourier analysis of different methods when the motor operates at 700 r/min. (a) With the traditional method. (b) With the proposed method. (c) Speed ripple FFT analysis of the traditional method. (d) Speed ripple FFT analysis of the proposed method.

To verify the effectiveness of the proposed method, Fig. 13 shows the experimental comparison results of speed ripple reduction when the motor operates at 700 r/min using the traditional CFT based method and the proposed method. The 2nd harmonic component is intentionally injected into the speed loop. It can be seen from Fig. 13(a) that the speed ripple increases by 36 r/min after enabling the traditional method, and the overcurrent fault occurred due to erroneous compensation.

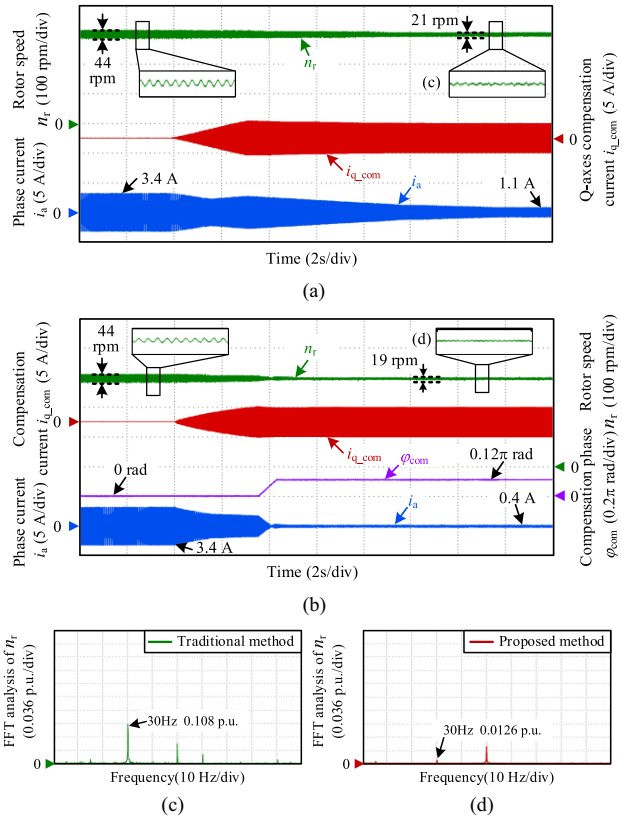

Fig. 14. Experimental comparison results and Fourier analysis of different methods when the motor operates at 300 r/min. (a) With the traditional method. (b) With the proposed method. (c) Speed ripple FFT analysis of the traditional method. (d) Speed ripple FFT analysis of the proposed method.

With the proposed method, as shown in Fig. 13(b), when the saturation issue is detected, the compensation angle is adaptively adjusted by 0.23π rad. The result is consistent with the conclusion of phase lag introduced by velocimetry in (3). The current amplitude decreases from 4.6 to 1.0 A, and the speed ripple is reduced by 11 r/min. Additionally, FFT comparison analysis of the speed ripple between two methods, as shown in Fig. 13(c) and (d), reveals that the 2nd harmonic content in the rotor speed decreases from 0.141 to 0.014 p.u. The proposed method achieves phase adaptive adjustment under the condition of erroneous speed ripple compensation.

Fig. 14 shows the experimental comparison results of speed harmonic suppression when the motor operates at 300 r/min using two methods. It can be seen from Fig. 14(a) that, the speed ripple decreases from 44 r/min to 21 r/min and the current amplitude decreases from 3.4 to 0.4 A after enabling the traditional method. However, the speed convergence process is slow. As shown in Fig. 14(b), the compensation angle adaptively adjusted by 0.12π rad to accelerate the convergence process with the proposed method. Also, the compensation angle is consistent with the conclusion of phase lag introduced by velocimetry in (3). The current amplitude decreased from 3.4 to 0.4 A, and the speed ripple was reduced by 25 r/min. FFT comparison analysis of the speed ripple between two methods, as shown in Fig. 14(c) and (d), reveals that the 2nd harmonic content in the rotor speed decreases from 0.108. to 0.0126 p.u. Based on

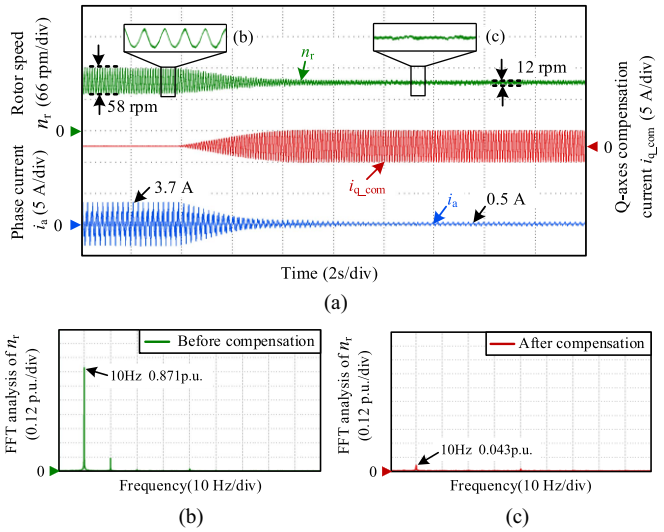

Fig. 15. Experimental results of the proposed method at 100 r/min. (a) Speed ripple reduction effect with the proposed method. (b) Speed ripple FFT analysis before compensation. (c) Speed ripple FFT analysis after compensation.

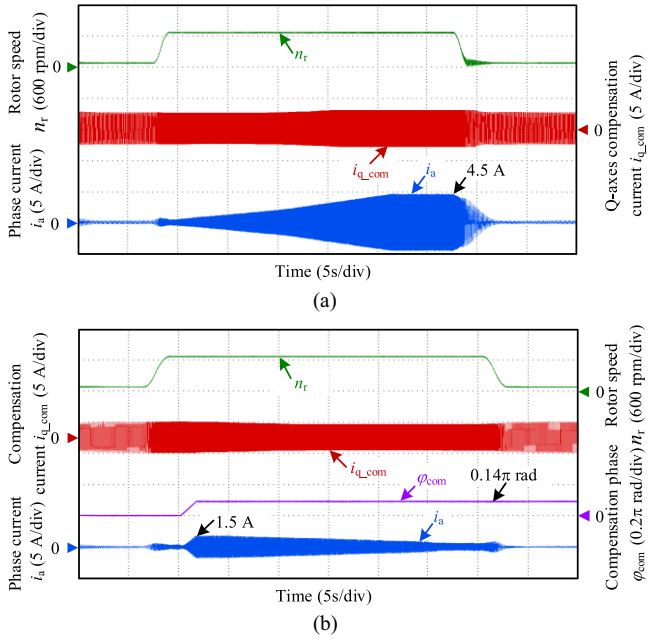

Fig. 16. Experimental results under varying speed conditions. (a) With the traditional method. (b) With the proposed method.

the above analysis, the proposed strategy not only adaptively corrects phase lag but also accelerates the speed ripple reduction convergence process, enhancing the algorithm's rapidity.

Fig. 15 shows the experimental result of speed harmonic suppression when the motor operates at 100 r/min with the proposed method. It can be seen that the speed ripple decreases from 58 r/min to 12 r/min after enabling the proposed method. Additionally, FFT analysis of the speed ripple reduction, as shown in Fig. 15(b) and (c), reveals that the 2nd harmonic content in the rotor speed decreases from 0.871 to 0.043 p.u. With minimal phase lag, no erroneous extraction occurs, indicating that the proposed strategy exhibits excellent stability at low-speed region.

To verify the effectiveness under varying speed conditions, Fig. 16 shows the experimental comparison between two methods in the speed range of 100 to 750 r/min. It can be seen from Fig. 16(a) that the current gradually diverges to 4.5 A as the motor accelerates to 750 r/min, indicating erroneous compensation with the traditional method. After applying the proposed method, as shown in Fig. 16(b) the compensation angle is adaptively adjusted by 0.14π rad and the maximum ripple current amplitude is 1.5 A. Therefore, the proposed method's control performance is superior to that of the traditional method.

To compare the control performance between the proposed method and the extended state observer (ESO) based method in [31], Fig. 17 shows experimental results of speed ripple reduction with the ESO based method. In Fig. 17(a), the speed ripple increases by 35 r/min after enabling the ESO based method when the motor operates at 100 r/min. However, in Fig. 17(b), the speed ripple increases by 7 r/min after enabling the ESO based method. The harmonic content in the speed is still high. The ESO based method in has a certain degree of rapidity in speed ripple reduction. However, as the harmonic frequency increases, the suppression effect gradually becomes worse. Comparing to the speed ripple reduction effect with the proposed method

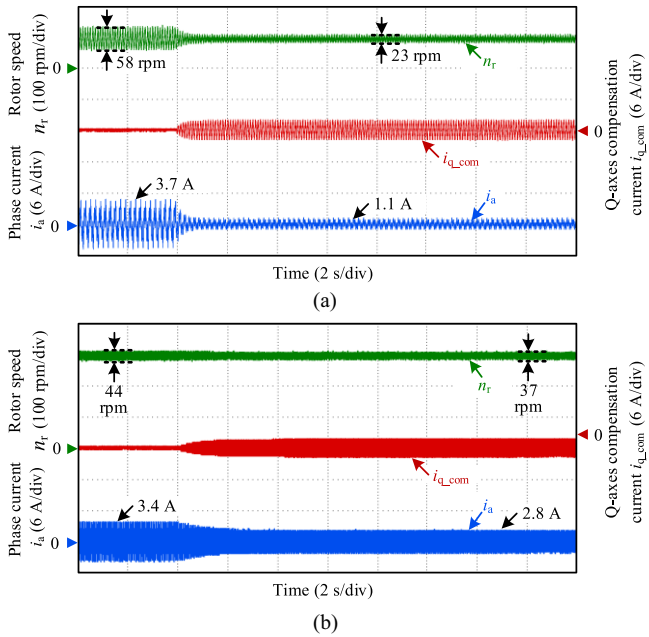

Fig. 17. Experimental results with the extended state observer based method. (a) 100 r/min. (b) 300 r/min.

in Figs. 14(b) and 15(a), the speed ripple reduction effect of proposed method is better than that of the ESO based method in full speed range.

To verify the effectiveness of the proposed method under 0%, 50% and 100% load conditions. Fig. 18(a) and (b) shows the experimental verification of the speed ripple reduction effect when the motor operates at 100 r/min and 750 r/min with load changes. It can be seen that the proposed method

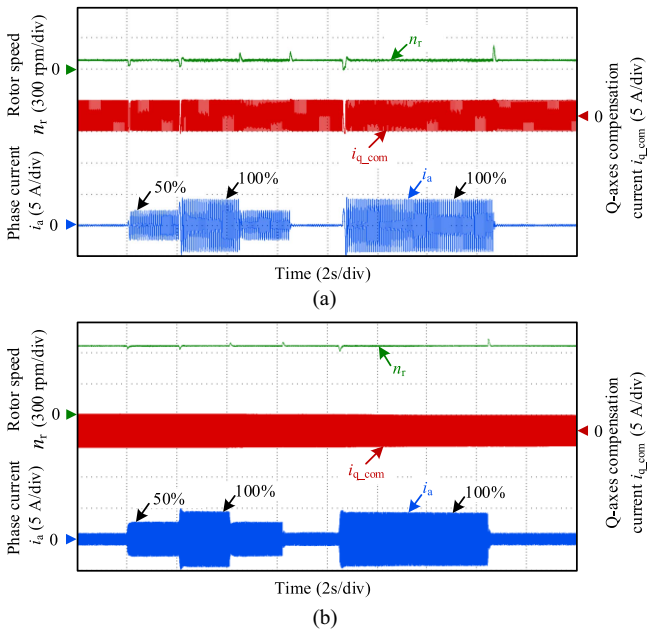

Fig. 18. Experimental results under 100% rated load, 50% rated load, and no-load conditions. (a) 100 r/min. (b) 750 r/min.

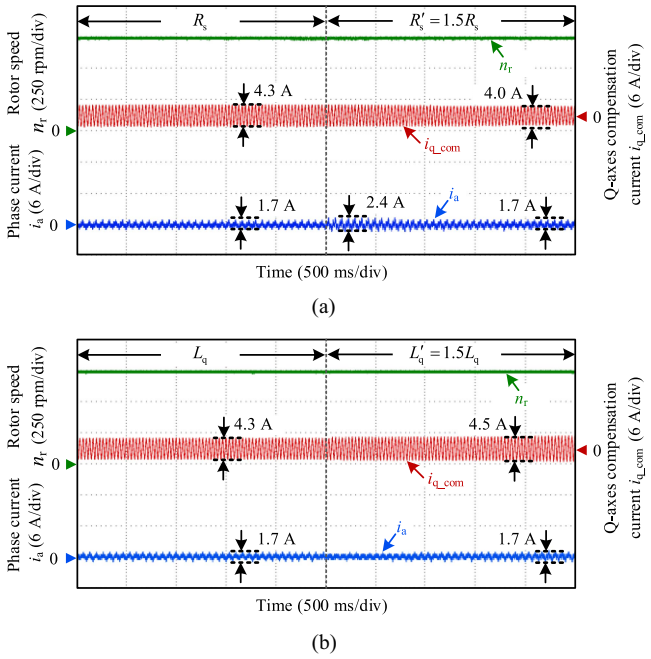

Fig. 19. Experimental results when motor parameters mismatch. (a) Resistance changes 50%. (b) Inductance changes 50%.

has good stability under different speeds and loads conditions, and speed ripple reduction ability is not affected by load changes.

To verify the robustness of the proposed algorithm, Fig. 19 shows the experimental results of the speed ripple reduction effect with the proposed method under the conditions of 50% resistance and inductance error. As can be seen from Fig. 19(a) that, under the condition of 50% resistance error, the q-axis

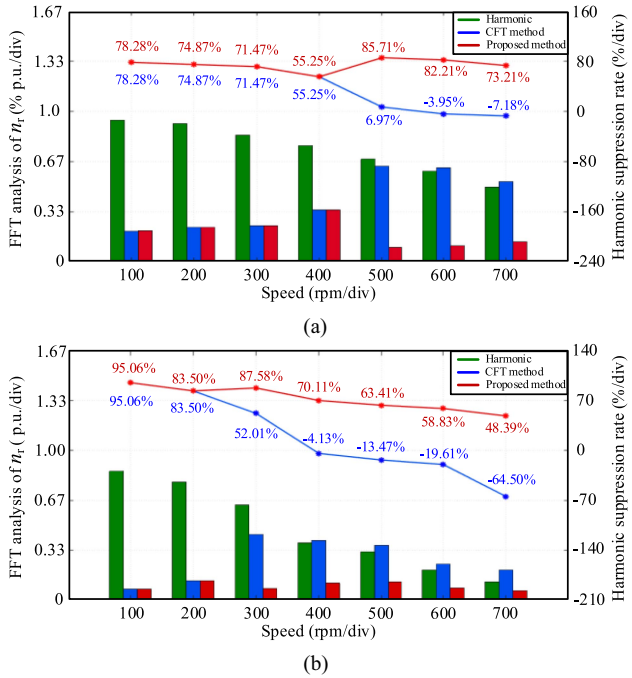

Fig. 20. Statistical chart of harmonic suppression under different conditions. (a) Fundamental frequency ripple. (b) 2nd harmonic ripple.

compensation current $i_{q\cdot com}$ is adaptively adjusted by 0.3 A without affecting the speed. Also, in Fig. 19(b), under the condition of 50% inductance error, the proposed method is minimally affected by the parameter changes. Therefore, the proposed algorithm works well in the condition of parameter mismatch.

Fig. 20 shows the statistical chart of harmonic suppression effects using two methods under rotor speeds ranging from 100 to 700 r/min. When the speed ripple harmonic at the mechanical speed ω_m, it can be seen from Fig. 20(a) that the proposed phase self-adjustment is enabled at 500 r/min when the system has fundamental frequency ripple, achieving a maximum harmonic suppression rate of 85.71%, and the suppression effect is superior to that of the traditional method. When the 2nd harmonic ripple is introduced, as shown in Fig. 20(b), the phase self-adjustment is enabled at 300 r/min, achieving a maximum harmonic suppression rate of 95.06%. In summary, the proposed method demonstrates excellent reduction effects on speed ripple and good generality.

V. Conclusion

A speed ripple reduction method based on adaptive harmonic tracking for PMSM drives has been proposed in this article. The proposed method utilizes the saturation characteristics of spectral analysis theory under unstable states to adaptively correct the injected harmonic modes. This method does not require distinguishing the sources of speed ripple, avoiding the complexity of parameter and convergence design in the model-based methods. Meanwhile, the proposed method is unaffected by the speed loop bandwidth and phase lag introduced by speed measurement,

offering advantages such as simple structure and strong versatility, and provides an effective solution for the high-performance harmonic injection–based speed ripple reduction method. The stability of the proposed method across three modes is analyzed with the Lyapunov theory. Additionally, the parameter tuning process is investigated, enhancing the ability to reduce speed ripple under various conditions. Although the proposed method includes the harmonic amplitude tracking, adaptive phase correction, and compensation current reconstruction functions, it does not increase much calculation load on the chip. Experimental results on the PMSM drives verify the effectiveness of the proposed method.

REFERENCES

[1] C. Zhang, C. Gan, K. Ni, Z. Yu, S. Wang, and R. Qu, "Computationally efficient cascaded predictive control for hybrid-inverter fed open-winding PMSM drive with fast partial preselection," *IEEE Trans. Power Electron.*, vol. 39, no. 3, pp. 3509–3520, Mar. 2024.

[2] M. S. Rafaq, W. Midgley, and T. Steffen, "A review of the state of the art of torque ripple minimization techniques for permanent magnet synchronous motors," *IEEE Trans. Ind. Inform.*, vol. 20, no. 1, pp. 1019–1031, Jan. 2024.

[3] G. Zhang et al., "Adaptive step-size predictive PLL based rotor position estimation method for sensorless IPMSM drives," *IEEE Trans. Power Electron.*, vol. 39, no. 5, pp. 6136–6147, May 2024.

[4] G. Wang, M. Valla, and J. Solsona, "Position sensorless permanent magnet synchronous machine drives—A review," *IEEE Trans. Ind. Electron.*, vol. 67, no. 7, pp. 5830–5842, Jul. 2020.

[5] Y. Zuo, C. Lai, and K. L. V. Iyer, "A review of sliding mode observer based sensorless control methods for PMSM drive," *IEEE Trans. Power Electron.*, vol. 38, no. 9, pp. 11352–11367, Sep. 2023.

[6] Y. Liu et al., "Three-vector-based model predictive torque control for dual three-phase PMSM with torque and flux ripples reduction," *IEEE Trans. Power Electron.*, vol. 39, no. 8, pp. 10009–10020, Aug. 2024.

[7] G. Zhang, G. Wang, D. Xu, and N. Zhao, "ADALINE-network-based PLL for position sensorless interior permanent magnet synchronous motor drives," *IEEE Trans. Power Electron.*, vol. 31, no. 2, pp. 1450–1460, Feb. 2016.

[8] G. Wang, R. Yang, and D. Xu, "DSP-based control of sensorless IPMSM drives for wide-speed-range operation," *IEEE Trans. Ind. Electron.*, vol. 60, no. 2, pp. 720–727, Feb. 2013.

[9] C. Yang, B. Song, Y. Xie, S. Zheng, and X. Tang, "Adaptive identification of nonlinear friction and load torque for PMSM drives via a parallel-observer-based network with model compensation," *IEEE Trans. Power Electron.*, vol. 38, no. 5, pp. 5875–5897, May 2023.

[10] J. Yang, W. Chen, S. Li, L. Guo, and Y. Yan, "Disturbance/uncertainty estimation and attenuation techniques in PMSM drives—A survey," *IEEE Trans. Ind. Electron.*, vol. 64, no. 4, pp. 3273–3285, Apr. 2017.

[11] G. Zhang et al., "Hybrid pseudorandom signal injection for position sensorless SynRM drives with acoustic noise reduction," *IEEE Trans. Transp. Electrific.*, vol. 8, no. 1, pp. 1313–1325, Mar. 2022.

[12] J. Qu, X. Li, F. Gao, C. Zhang, and P. Zhang, "Torque ripple reduction of permanent magnet synchronous machine drives with tangential vibration acceleration control," *IEEE Trans. Power Electron.*, vol. 40, no. 4, pp. 4902–4913, Apr. 2025.

[13] J. Qu, P. Zhang, and J. Jatskevich, "Harmonic current optimization for torque ripple reduction in permanent magnet synchronous machine drives based on torque ripple surrogate model," *IEEE Trans. Power Electron.*, vol. 39, no. 5, pp. 5108–5120, May 2024.

[14] W. Jiang et al., "A novel stator wound field flux switching machine with the combination of overlapping armature winding and asymmetric stator poles," *IEEE Trans. Ind. Electron.*, vol. 69, no. 3, pp. 2737–2748, Mar. 2022.

[15] J. Liang, A. Parsapour, Z. Yang, C. Caicedo-Narvaez, M. Moallem, and B. Fahimi, "Optimization of air-gap profile in interior permanent-magnet synchronous motors for torque ripple mitigation," *IEEE Trans. Transp. Electrific.*, vol. 5, no. 1, pp. 118–125, Mar. 2019.

[16] K. Yamazaki and Y. Seki, "Zeroization of cogging torque of permanent magnet machines by optimizing rotor surface shape: Comparison between surface and interior types," *IEEE Trans. Magn.*, vol. 59, no. 5, May 2023, Art. no. 8100904.

[17] F. Bu et al., "Speed ripple reduction of direct-drive PMSM servo system at low-speed operation using virtual cogging torque control method," *IEEE Trans. Ind. Electron.*, vol. 68, no. 1, pp. 160–174, Jan. 2021.

[18] G. Zhang et al., "PR internal mode extended state observer-based iterative learning control for thrust ripple suppression of PMLSM drives," *IEEE Trans. Power Electron.*, vol. 39, no. 8, pp. 10095–10105, Aug. 2024.

[19] Z. Tang and B. Akin, "Suppression of dead-time distortion through revised repetitive controller in PMSM drives," *IEEE Trans. Energy Convers.*, vol. 32, no. 3, pp. 918–930, Sep. 2017.

[20] M. Tian, B. Wang, Y. Yu, Q. Dong, and D. Xu, "Discrete-time repetitive control-based ADRC for current loop disturbances suppression of PMSM drives," *IEEE Trans. Ind. Inform.*, vol. 18, no. 5, pp. 3138–3149, May 2022.

[21] G. Lee, S. Kim, J. Hong, and J. Bahn, "Torque ripple reduction of interior permanent magnet synchronous motor using harmonic injected current," *IEEE Trans. Magn.*, vol. 44, no. 6, pp. 1582–1585, Jun. 2008.

[22] Z. Wu, Z. Yang, K. Ding, and G. He, "Transfer mechanism analysis of injected voltage harmonic and its effect on current harmonic regulation in FOC PMSM," *IEEE Trans. Power Electron.*, vol. 37, no. 1, pp. 820–829, Jan. 2022.

[23] L. Wu and Z. Lyu, "Harmonic injection-based torque ripple reduction of PMSM with improved dc-link voltage utilization," *IEEE Trans. Power Electron.*, vol. 38, no. 7, pp. 7976–7981, Jul. 2023.

[24] G. Liu, B. Chen, K. Wang, and X. Song, "Selective current harmonic suppression for high-speed PMSM based on high-precision harmonic detection method," *IEEE Trans. Ind. Inform.*, vol. 15, no. 6, pp. 3457–3468, Jun. 2019.

[25] X. Wang, C. Jiang, F. Zhuang, C. H. T. Lee, and C. C. Chan, "A harmonic injection method equivalent to the resonant controller for speed ripple reduction of PMSM," *IEEE Trans. Ind. Electron.*, vol. 69, no. 10, pp. 9793–9803, Oct. 2022.

[26] Y. Bai, G. Zhang, G. Wang, F. Chen, G. Bi, and D. Xu, "Position and speed detection method based on adaptive extended moving-window linear regression for traction machine drives," *IEEE Trans. Transp. Electrific.*, vol. 8, no. 2, pp. 2884–2897, Jun. 2022.

[27] Y. Chen, M. Yang, J. Long, D. Xu, and F. Blaabjerg, "M/T method based incremental encoder velocity measurement error analysis and self-adaptive error elimination algorithm," in *Proc. 43rd Annu. Conf. IEEE Ind. Electron. Soc.*, 2017, pp. 2085–2090.

[28] A. Wireko-Brobby, Y. Hu, G. Wang, C. Gong, W. Lang, and Z. Zhang, "Analysis of the sources of error within PMSM-based electric powertrains—A review," *IEEE Trans. Transp. Electrific.*, vol. 10, no. 3, pp. 6370–6406, Sep. 2024.

[29] Y. Vázquez-Gutiérrez, D. L. O'Sullivan, and R. C. Kavanagh, "Small-signal modeling of the incremental optical encoder for motor control," *IEEE Trans. Ind. Electron.*, vol. 67, no. 5, pp. 3452–3461, May 2020.

[30] S. Wang et al., "Torque disturbance compensation method based on adaptive Fourier-transform for permanent magnet compressor drives," *IEEE Trans. Power Electron.*, vol. 38, no. 3, pp. 3612–3623, Mar. 2023.

[31] H. Wang, Y. Zuo, C. Zhao, H. Cao, and C. H. T. Lee, "Improved disturbance rejection ability for speed control of PMSM drives using a modified cascaded extended state observer," *IEEE J. Emerg. Sel. Topics Power Electron.*, vol. 13, no. 2, pp. 1580–1590, Apr. 2025.

[32] A. Apte, V. A. Joshi, H. Mehta, and R. Walambe, "Disturbance-observer-based sensorless control of PMSM using integral state feedback controller," *IEEE Trans. Power Electron.*, vol. 35, no. 6, pp. 6082–6090, Jun. 2020.

[33] J. Yim, S. You, Y. Lee, and W. Kim, "Chattering attenuation disturbance observer for sliding mode control: Application to permanent magnet synchronous motors," *IEEE Trans. Ind. Electron.*, vol. 70, no. 5, pp. 5161–5170, May 2023.

[34] S. Li and H. Gu, "Fuzzy adaptive internal model control schemes for PMSM speed-regulation system," *IEEE Trans. Ind. Inform.*, vol. 8, no. 4, pp. 767–779, Nov. 2012.

Siqi Wang received the B.S. and M.S. degrees in electrical engineering from the Nanjing University of Aeronautics and Astronautics, Nanjing, China, in 2018 and 2021, respectively. He is currently working toward the Ph.D. degree in power electronics and electrical drives with the Harbin Institute of Technology, Harbin, China.

His research interests include advanced control of permanent magnet synchronous motor drives and position sensorless control of ac motors.

Binxing Li (Member, IEEE) received the B.S. degree in electrical engineering from the Harbin Institute of Technology, Weihai, China, in 2017. He is currently working toward the Ph.D. degree in power electronics and electrical drives with the Harbin Institute of Technology, Harbin, China.

His research interests include permanent magnet synchronous motor drives, high efficiency ac–dc converters, and the application of GaN power devices.

Guoqiang Zhang (Senior Member, IEEE) received the B.S. degree in electrical engineering from Harbin Engineering University, Harbin, China, in 2011, and the M.S. and Ph.D. degrees in electrical engineering from Harbin Institute of Technology, Harbin, China, in 2013 and 2017, respectively.

Since 2017, he has been with the Department of Electrical Engineering, Harbin Institute of Technology, where he is currently an Associate Professor. His research interests include control of electrical drives and parameter identification techniques, with the main focus on sensorless field-oriented control of synchronous motor drives.

Dr. Zhang is an Associate Editor for the *Journal of Power Electronics*.

Gaolin Wang (Senior Member, IEEE) received the B.S., M.S., and Ph.D. degrees in electrical engineering from Harbin Institute of Technology, Harbin, China, in 2002, 2004, and 2008, respectively.

In 2009, he joined the Department of Electrical Engineering, Harbin Institute of Technology as a Lecturer, where he has been a Full Professor of Electrical Engineering since 2014. From 2009 to 2012, he was a Postdoctoral Fellow with Shanghai Step Electric Corporation, where he was involved in the traction machine control for direct-drive elevators. He authored more than 60 technical papers published in IEEE Transactions. He is the holder of 30 Chinese patents. His research interests include permanent magnet synchronous motor drives, position sensorless control of ac motors, and digital control of power converters.

Dr. Wang is a Guest Associate Editor for IEEE TRANSACTIONS ON INDUSTRIAL ELECTRONICS, an Associate Editor for IEEE TRANSACTIONS ON TRANSPORTATION ELECTRIFICATION, *IET Electric Power Applications*, and *Journal of Power Electronics*.

Jianbing Chen received the B.S. degree in mechatronic engineering from the University of Electronic Science and Technology of China, Chengdu, China, in 2002.

He was with Hisense Air Conditioning Company Ltd. and Magene Tech Company Ltd., engaging in the research and development of variable frequency air conditioners and smart cycling product controllers, respectively. He holds more than 100 invention patents. He is currently with Qingdao Innovation Intelligent Appliance Research Institute Company Ltd., focusing on the research and development of high-end smart home appliance controllers. His research interests include the application of new power devices and the research and application of core algorithms for variable frequency control in home appliances.

Mr. Chen was awarded the title of Senior Engineer (Professor Level) in the field of Engineering Technology by the Shandong Provincial Department of Industry and Information Technology in 2023.

Jiangtao Yu received the B.S. degree in electronic information engineering from Qingdao Agricultural University, Qingdao, China, in 2009.

He is currently working toward algorithmic controls in power electronics and electrical drives with the National Innovation Institute of High-end Smart Appliances, China. His research interests include permanent magnet synchronous motor drives and PMa-SynRM position sensorless control.

Dianguo Xu (Fellow, IEEE) received the B.S. degree in control engineering from Harbin Engineering University, Harbin, China, in 1982, and the M.S. and Ph.D. degrees in electrical engineering from the Harbin Institute of Technology (HIT), Harbin, China, in 1984 and 1989, respectively.

In 1984, he joined the Department of Electrical Engineering, HIT, as an Assistant Professor. Since 1994, he has been a Professor with the Department of Electrical Engineering, HIT. From 2000 to 2010, he was the Dean of the School of Electrical Engineering and Automation, HIT, and the Assistant President from 2010 to 2014. He is currently the Vice-President of the HIT. He authored or coauthored more than 600 technical papers. His research interests include renewable energy generation technology, power quality mitigation, sensorless vector-controlled motor drives, and high-performance permanent magnet synchronous motor servo systems.

Dr. Xu is the Chair of IEEE Harbin Section, the Co-EIC of IEEE TRANSACTIONS ON POWER ELECTRONICS, an Associate Editor for IEEE TRANSACTIONS ON INDUSTRIAL ELECTRONICS and IEEE JOURNAL OF EMERGING AND SELECTED TOPICS IN POWER ELECTRONICS. He was the recipient of the 2018 IEEE IAS Outstanding Achievement Award.